A Novel Whale Optimized TGV-FCMS Segmentation with Modified LSTM Classification for Endometrium Cancer Prediction

T. Satya Kiranmai[1] and P.V.Lakshmi[2] ,

tadepallikiranmai84@gmail.com

Department of Information Technology, Chaitanya Bharathi Institute of Technology (A), Hyderabad, India.
Professor, Department of CSE GITAM (Deemed to be University) Visakhapatnam, India.

Abstract

Early detection of endometrial carcinoma in uterus is essential for effective treatment. Endometrial carcinoma is the worst kind of endometrium cancer among the others since it is considerably more likely to affect the additional parts of the body if not detected and treated early. Non-invasive medical computer vision, also known as medical image processing, is becoming increasingly essential in the clinical diagnosis of various diseases. Such techniques provide a tool for automatic image processing, allowing for an accurate and timely assessment of the lesion. One of the most difficult aspects of developing an effective automatic categorization system is the absence of huge datasets. Using image processing and deep learning, this article presented an artificial endometrium cancer diagnosis system. The processes in this study include gathering a dermoscopy images from the database, preprocessing, segmentation using hybrid Fuzzy C-Means (FCM) and optimizing the weights using the Whale Optimization Algorithm (WOA). The characteristics of the damaged endometrium cells are retrieved using the feature extraction approach after the Magnetic Resonance pictures have been segmented. The collected characteristics are classified using a deep learning-based methodology called Long Short-Term Memory (LSTM) and Bi-directional LSTM classifiers. After using the publicly accessible data set, suggested classifiers obtain an accuracy of 97% and segmentation accuracy of 93%.

Keywords:
Dermoscopy Image; Deep Learning; Fuzzy C-Means; Long Short Term Memory; Endometrium Cancer Detection; Whale Optimization Technique.

1. Introduction

Endometrial cancer is one of the most common gynecological cancers in developed nations. More women are being diagnosed with endometrial cancer than ever before [1,2]. A layer of the uterine wall called myometrium acts as a defense against the spread of endometrial cancer [3,4]. Poor prognoses might be predicted if the illness is discovered at an advanced stage. Is myometrial invasion depth a key factor in diagnosing the stage of the disease? This is a predictive factor used to put patients into high or low–intermediate risk groups, which leads to distinct postoperative treatment options [5]. As a result, the key to a positive prognosis is early and correct diagnosis, followed by proper therapy. Endometrial cancer myometrial invasion depth is now best assessed with magnetic resonance imaging (MRI) [9–11]. MRI is the gold standard in this area. There is a growing trend in the medical field of using artificial intelligence (AI) in the interpretation of medical pictures [12, 14].

When it comes to radiology, artificial intelligence (AI) is a great fit since MRI images may be measurable, making it ideal for AI. The categorization system subdiscipline makes use of several techniques, such as the artificial neural network (ANN). Deep learning (DL) has gotten a lot of interest in the field of ANN recently. Sub-algorithms for rapid processing, memory improvement, and new model features and designs are always being created and improved. Most often employed by DL is the convolutional neural network, which is the most appropriate neural network for radiography when pictures are the main unit of analysis [15,16]. CNN is a biologically inspired network that mimics the behavior of the brain cortex, which has a complex structure of cells sensitive to tiny parts of the visual field. The CNN is not just a collection of layers that map image inputs to desired end locations, but it also learns higher-level imaging properties. [17]

Gynecological cancers are diagnosed, staged, and classified using MRI scans, which are often utilized in clinical settings. [7–9]. The sensitivity (SEN) and specificity (SPE) of MRI's depth assessment findings ranged from 42 to 100% and 85 to 93%, respectively. Tumor volume assessment on ECM has been linked to deep MI and lymph node metastases (LNMs) in recent studies and may be considered a bad prognostic sign for EC patients [10–13]. Deep MI may be predicted with

good accuracy (ACC) if the tumor-uterine volume ratio is more than 25% [13]. For deep MI diagnosis, quantitative measures on MRI are more accurate than direct observation, although it might be erroneous to evaluate an EC lesion that is not evident on the scan. Deep MI assessment was analyzed using an MRI-based texture model that generated a SEN and SPE of 79.3 percent and 82.3 percent, respectively [14]. To present, reported research have demonstrated that the SEN and SPE for MI assessment on ECM are underwhelming. The findings mostly dependent on manual cancer volume computation and individual interpretation, which differed depending on both institutional modes and operators' expertise. The lack of consistency in assessment has a negative impact on its use in clinical settings. For MI assessment, intraoperative frozen section is another alternative, however the results are less reliable than the final pathological diagnosis [15]. Deep learning using convolutional neural networks (CNNs) is a novel approach of computer-aided diagnosis that enables automated capture of the targeted region following the training process [16–22]. The use of DL on ECM to automatically determine MI depth has not yet been studied, as far as we know. From this perspective, the goal of this study was twofold: first, we attempted to establish a machine learning (ML) network to automatically determine MI depth on T2WI-based ECM using DL method with sufficient training data that had known MI status labels; second, we compared the evaluation of computerized network learning model with radiologists' results in judging MI depth.

As defined by the International Federation for Gynecology and Obstetrics, Stage IA and IB are two distinct categories of endometrial cancer depending on the degree of myometrial invasion (less than vs. more than 50% myometrial invasion) in Stage I [6]. But the ability to estimate the preoperative MRI phases relies heavily on individual knowledge and experience, which varies from person to person [18]. Other pathogenic reasons that might contribute to an inaccurate diagnosis of myometrial invasion include hematometra, interference from an existing large leiomyoma or adenomyosis, and variations in the histological subtypes of endometrial cancer [10,19]. The pre-operative MRI staging, and post-operative pathological staging typically differ. Endometrial cancer diagnosis relies heavily on the performance of CNN-based classifiers for "post-operative" diagnosis, whereas research on "preoperative" MRI staging and performance of AI interpretation on endometrial cancer is rather uncommon [20]. There has

been little research into whether AI may aid clinicians with pre-operative diagnosis, or diagnosing MRI before surgery, and our work is the first to look at this possibility. This was accomplished by testing the diagnosis accuracy of the DL model for myometrial invasion vs that of radiologists. At an early stage, we utilized CNN to determine the depth of endometrial cancer invasion and explored the implications of employing AI as an auxiliary resource for generating more complete judgments, as seen below.

Some key issues are discussed as follows in current methodologies:

- ❖ A significant disadvantage of contemporary technology consists of the premature conclusion of the edge/no edge. To identify an extended contour with very low contrast, a very low threshold needs to be established. This inevitably leads to random edge sections being identified in the image, making it more difficult to analyze curvilinear links than when the contrast data is raw.
- ❖ In some computer-aided systems, picture processing and segmentation components are left out. The texture function is collected from the image or ROI immediately and is used as inputs to the classifier system in these models. Such a computer-aided system is straightforward and computer complicated. However, functionality taken straight from ROIs cannot support robust and accurate implementation.
- ❖ The useful information, like the micro-calcification and masses in endometrium picture, is exceedingly difficult to discern at its early stage because of a low level of contrast and noise. The problem of lack of data arises when the photographs are poorly directed.

The rest of the paper is decided as follows. Section 2 deliberates the works that are linked to ours. Section 3 introduces the suggested methods for endometrium cancer uncertainty prediction. Section 4 delves deeply into the acquired results and simulations. Finally, in section 5, the study is brief with a conclusion and future work.

2. Literature review

These breakthroughs in artificial intelligence (AI) and machine learning (ML) allow the use of these sophisticated approaches in healthcare, while also enhancing the performance and accuracy criteria set by conventional statistical techniques [23]. Many ML algorithms have previously been used to clinical data to study a wide range of disorders and therapeutic areas, their start, progression, and therapy choices [1]. Medical picture data may also be used to forecast illness start and development with improved accuracy using deep learning techniques like convolutional neural network (CNN) [24, 25].

Machine learning (ML) algorithms used to enormous amounts of organized and unstructured data have already helped academics mine the vast amounts of data and make patient healthcare choices [26]. With the superior precision and robustness of machine learning algorithms compared to more conventional statistics, these insights have become critical in guiding healthcare access, patient care, disease diagnosis, healthcare trend forecasting and drug discovery efforts, among other things. This has a positive impact on medical costs and a corresponding reduction in the time it takes for diagnosis.

Among women of childbearing age, endometriosis is a frequent ailment. Endometrium-like tissue grows on the outer surface of the uterus and other pelvic organs. There is a wide range of signs and symptoms among patients, with some showing minor symptoms and others showing moderate to severe indicators. These include discomfort in the pelvic region, dysmenorrhea, and inability to bear children as the most prevalent symptom of endometriosis. Endometriosis is often diagnosed using laparoscopy, which is a surgical procedure done under general anesthesia [28]. The fact that it is an intrusive treatment means that not all women are good candidates for it. Laparoscopy is a costly operation, and women must have a range of indicators of endometriosis before having it [29]. Endometriosis biomarkers are also being investigated by examining endometrial tissue, uterine or menstrual fluids, immunological markers in blood or urine, gene expressions, and other methods [30].

Many unnecessary surgeries and their associated risks might be avoided if noninvasive technologies were available to forecast the probability of endometriosis [31]. This would minimize diagnostic delays and the number of women who have surgery. Genome Forest, a novel ensemble approach created by academics, was used to evaluate gene expression data in other investigations.

Using both transcriptomics and methylomics data, the technique rigorously tested its ability to distinguish endometriosis and control samples.

Endometriosis risk may be predicted using logistic regression in another study based on symptoms (LR). A 25-item self-administered questionnaire was used to gather symptomatic data, including demographics, prior medical history, obstetrics, and family history [34]. It has been determined that the use of ultrasonography in the diagnosis of endometriosis should continue to be the first-line approach in the assessment of patients with the disease [35].

Researchers have been working on CNN-based CAD systems to categorize hysteroscopy pictures of endometrial lesions and assess the model's diagnostic performance in recent years [36]. Classifying endometrial lesion photos, their method outperformed gynecologists by a margin. Endometriosis may be diagnosed using a wide range of tests, but there is currently no confirmed cure for the condition. Patients may be able to benefit from early diagnosis and accessible medicinal and surgical alternatives, however, which may help to lower the risk of problems and enhance their quality of life.

In the studies, researchers developed models or algorithms to predict the risk of endometriosis based on small samples or a restricted number of factors. Most of the data came from clinics and other health care facilities that operated in a strictly regulated setting. For endometriosis prediction, there has been a limited amount of study based on US patient-level claims data. Information about a patient's whole medical history is included in the data collected by the insurance company [39, 40]. Use of patient-level transactional data from the United States was used to construct accurate machine learning algorithms to predict the beginning of endometriosis. By using a patient's medical history to predict the likelihood of endometriosis development, diagnostics and patient quality of life might be enhanced. It was shown that endometriosis onset was caused by factors that could be detected using the LR and Extreme Gradient Boosting (XGB) algorithms.

3. Proposed system

In this section, the four major steps are used, where the input images are taken from two publicly available datasets. Segmentation of the tumor is done using pre-processing techniques. The segmentation is conducted by Total Generalized Variation based FCM (TGVFCMS), where the weights of TGVFCMS is optimized by

modified WOA. The features are extracted and given as input for classifiers for final endometrium cancer prediction. The following Figure 1 shows the working flow of the projected methodology.
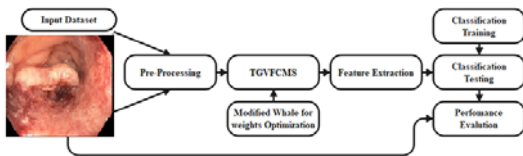

Fig. 1. Proposed Architecture.

3.1. Data set

This is a retrospective study obtained data from PLCO data set of 64 surgically treated endometrial cancer patients. At the Tri-Service General Hospital in Taipei, Taiwan, between January 2017 to September 2021, 172 people had surgery. For this study, we eliminated patients who had their endometrial cancer staged based solely on post-operative pathology and those with stage II, III, and IV cancers. In the end, this research included 64 eligible patients. Based on permanent pathology, 53 of these patients were found to have cancer in the stage IA stage, while 19 were found to have cancer in the stage IB stage. Patients ranged in age from 39 to 85, with an average age of 59.7. According to menopausal status, 88.5 percent of the population is postmenopausal. 27, 32, and 13 were classified as histology grades 1, 2, and 3 respectively (5 were serous carcinomas, one was clear cell, and 3 were mixed). 29 (40.3%) of the patients had uterine leiomyomas, whereas 43 (59.7%) did not.

These 64 patients provided a total of 4563 MRI slices (3242 contrast enhanced T1w slices and 1440 T2w slices) and complete preoperative radiology reports. Each patient was assigned to one of three groups: training, validation, or testing. The patients in the training group were those whose radiologists' diagnosis and pathology reports were consistent. Only 24 cases were chosen to train the DL model and create model parameters, which was a third of all patients. An independent validation group evaluated the error function to confirm that the model was performing as expected (6 patients). The model with the lowest error was chosen as the final

one. It was then utilized to evaluate the AI-based system's accuracy rate in a separate dataset of 42 patients (plus the six patients in the validation group) from the training group (see Section 3). Oncologists with 25 and 14 years of expertise, respectively, were recruited to classify the MRI scans of each patient, identifying the uterus's outlines, the lesion of the endometrium, and its lining. Our study team then double-checked their findings. It was necessary to label the AI model's picture segmentation and training using contrast enhanced T1w and T2w images. Results from the histopathology report were utilized as a basis for determining accuracy rates.
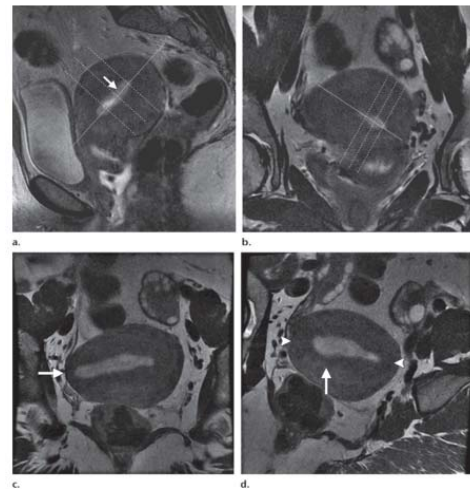

Fig.2. Dataset Sample images

3.2. Pre-processing

The suggested pre-processing includes two distinct steps: image improvement using the HLOG filter and Tumor detection and segmentation. The tumor detection and segmentation are a key step for developing a CAD system to diagnose malignant melanocytic lesions in the Magnetic Resonance image. Several techniques to tumor segmentation have been explored in the past [25-27]. However, most of these methods had not provided appropriate segmentation of tumors in endometrial. The suggested approach identifies tumors in the Magnetic Resonance picture with high accuracy. In compared to the green and red channels, the blue channel of the RGB picture vividly displays the tumor. The picture is then sharpened to boost its intensity by subtracting the HLOG filter Magnetic Resonance image from the 3x3 to mean-filtered image. Bottom hat transformations are then applied to the sharpened picture using a linear structuring element with

orientations ranging from 0 to 3600. To identify unevenly dispersed segmentations in the picture, the responses are averaged, and 1% of the reaction data is saturated at low and high intensities to improve contrast. To transform the intensity image into a binary image, a normalized intensity value in the variety [0 1] is realistic to the contrast-enhanced image. Fig. 3 demonstrations the images gained after the application of the overhead labeled procedure. Fig.3. a. Represents the Magnetic Resonance input image of PLCO data set. Fig.3. b. represents the Magnetic Resonance image tumor detected the image. Fig.3. c. Represents the HLOG filter output image
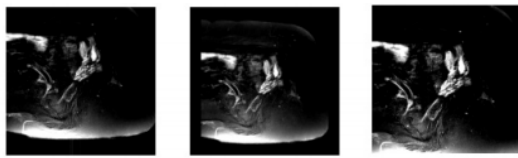
Fig.3. a   Fig.3. b   Fig.3. c

Figure 3: Sample images for Pre-processing

The Laplacian filters are by-product filters, and they are employed in Magnetic Resonance images to detect the areas of edges. These derivative filters are particularly sensible to noise and are therefore employed here to smoothen the dermoscope image with the Gaussian filters. The Gaussian filtration is employed again to smooth Magnetic Resonance images after these two steps. The LOG filter is displayed in eq. (1), and the Gaussian LOG filter is displayed in eq. (2).

The LoG scale-space illustration is

$$V^2 G(x,y) = \frac{x^2+y^2-2\sigma^2}{\pi\sigma^4} exp\left(\frac{-x^2+y^2}{2\sigma^2}\right) \quad (1)$$

$$G(x,y,\sigma) = \frac{1}{\sqrt{2\pi\sigma^2}} exp\left(\frac{-x^2+y^2}{2\sigma^2}\right) \quad (2)$$

3.3. Segmentation Using TGVFCMS

Magnetic Resonance pictures often include segments of normal endometrium as well as endometrium lesion segments. It is important to distinguish among normal and endometrium lesions to extract the characteristics properly. Segmentation methods can be used to identify endometrium lesions. One of the most significant characteristics of our TGVFCMS technique is its resistance to noise and ability to preserve edges. TGV regularization has favorable qualities up to a given level of differentiation, making it a valuable tool for measuring picture attributes such as noise removal and sharp edge preservation. TGV regularization was employed during

the smoothing period of our TGVFCMS to reduce undesirable noises and artifacts from FCM-based approaches [28]. First, let us define TGV as follows:

$$TGV_a^k(u) - sup\left\{\int_\Omega udiv^k vdx \mid v \in C_c^k(\Omega, Sym^k(R^d)), \|div^l v\|_\infty \le a_l\right\} \quad (3)$$

Where $l - 0,1,...,k-1$, and $k \in N$ specifies an order of TGV, and $a = (a_0, a_1,...,a_{k-1})$ designates the positive weight to TGV. $Sym^k(R^d)$ as k- tensors. For every single component $\eta \in M_{k-1}$, the l-d of the symmetric k tensor arena is given by

$$(div^l v)_\eta = \sum_{\gamma \in M_1} \frac{n!}{\gamma!} \frac{\partial^l v_{\eta+\gamma}}{\partial x^\gamma} \quad (4)$$

Where M_k is the multi-index of order k

$$M_k = \left\{\eta \in N^d \mid \sum_{i=1}^d \eta_i = k\right\} \quad (5)$$

The ∞- norm for symmetric k-vector field is assumed as

$$\|v\|_\infty = supx \in \Omega \left\{\left(\sum_{\eta \in M_k} \frac{k!}{\eta!} v_\eta(x)^2\right)\right\} \quad (6)$$

Both the first order and high-order gradients are restricted to be sparse, which can clearly decrease staircase artifacts. In this case, we consider the second order TGV, i.e.

$$TGV_a^2(u) = sup\left\{\int_\Omega udiv^2 vdx \mid v \in C_c^2(\Omega, S^{d\times d}), \|v\|_\infty \le a_0, \|div\, v\|_\infty \le a_1\right\} \quad (7)$$

Where $C_c^2(\Omega, S^{d\times d})$ signifies as the space vector of compactly sustained under the set of symmetric matrices $S^{d\times d}$. The relevant meanings and standards can be calculated as follows, in particular:

$$(div\, v)_i = \sum_{j=1}^d \frac{\partial v_{ij}}{\partial x_j}, \quad (div^2 v)_i = \sum_{j=1}^d \frac{\partial^2 v_{ii}}{\partial x_i^2} + 2 \sum_{k<j} \frac{\partial v_{ij}}{\partial x_i \partial x_j} \quad (8)$$

And

$$\|v\|_\infty = supx \in \Omega \left(\sum_{i=1}^d |v_{ii}(x)|^2 + 2\sum_{i<j} |v_{ij}(x)|^2\right)^{\frac{1}{2}}$$

$$\|div\, v\|_\infty = supx \in \Omega \left\{\sum_{i=1}^d \left|\sum_j^d \frac{\partial v_{ij}}{\partial x_j}(x)\right|^2\right\}^{\frac{1}{2}} \quad (9)$$

Where Ω the minimal solution is over all vector fields and $\varepsilon(v) = \frac{\nabla v + \nabla u\, T}{2}$ is the symmetrized derivative. In this

case, the definition of (9) demonstrates that 2 u contributes less to smooth areas than $\nabla u = v$. In therefore minimization might work well with $v = 0$. As a result, presents a method for achieving a balance between the first and second derivatives. The suggested TGVFCMS can produce consequences that are more resistant to noise and detail-conserving by defining second-order TGV [29-30]. Modified Whale for Weights Optimization is used to optimize those weight variables.

3.3.1. Modified Whale for weights Optimization

In this section, the WOA adjusts the standard to account for alternative approaches. There are three suggested amendments to the MWOA. Global metaheuristic computing suffers from a basic flaw: it tends to focus on the ideal neighborhood even when diversity decreases fast, and the first WOA is not a superior alternative. Levy flying courses have been widely employed in MA study to avoid near Optima agreements and accelerate integration while looking at global hunting productivity in the past That's why levies fly at MWOA to divert population diversity from its near-optimal state.

With a step length following the Lévy assumption, the Lévy flight is a non-Gaussian random practice with non-Gaussian results. The Lévy conveyance has a power-law vision.:

$$L(s) \sim |s|^{-1-\beta}, 0 < \beta \leq 2 \quad (10)$$

Where β an index, s is is the step length of the Lévy flight. Mantegna's procedure is applied to calculating

$$s = \mu / |\vartheta|^{1/\beta} \quad (11)$$

Where, μ And ϑ obey normal distribution, i.e.

$$\mu \sim N(0, \sigma_\mu^2), \vartheta \sim N(0, \sigma_\mu^2) \quad (12)$$

$$\sigma_\mu = \left[\frac{\tau(1+\beta).\sin(\pi\beta/2)}{\tau(\frac{1+\beta}{2}).\beta.2^{\frac{(\beta-1)}{2}}}\right]^{1/\beta} \quad (13)$$

$$\sigma_\vartheta = 1 \quad (14)$$

A step size avoiding the Lévy flight leaping out of the design field is adopted. It is defined by:

$$Levy = random(size(D)) \oplus L(\beta) \sim \frac{0.01\mu}{|v|^{\frac{1}{\beta}}(X_t - X^s)} \quad (15)$$

If the problem's size (D) is 1, the initial multiplication is 1 and the ith vector of the solution is Xi. It is common for the levy flight to create a long separation to improve research capacity, while a short separation is developed to improve performance due to the endless changes in the levy circulation. MA, of course, will return to the nearby town of Optima as a result of its legal status. As a replacement for the procurement tool, Levy's trip to better understand the research field at MWOA has been implemented. The novel's setting has also been modernized in this manner.

$$X(t+1) = X(t) + \frac{1}{sqrt(t)}.sign(rand - 0.5) \oplus Levy \quad (16)$$

Square root (t) and iteration number t are both represented by 1 / square root (t). If you are searching for anything specific, it's best to begin your search as soon as possible. Use Sign (rand-0.5) instead of the more often used rand function, which has just three potential values: -1, 0, and 1. An overview of the MWOA research is provided below.:

$$X(t+1) = \begin{cases} X(t) + \frac{1}{sqrt(t)}.sign(rand - 0.5) \oplus Levy & if\ p < 0.5 \\ D'.e^{bl}\cos(2\pi l) + X^s(t) & if\ p \geq 0.5 \end{cases} \quad (17)$$

Finally predicted two weights are applied in the α_0 and α_1. Which are basically it's turned around 0.1 and 0.15.

3.4. Feature extraction

The DWT, which takes into consideration the rectangular function, is used to compute the input coefficient of the input pictures. The DWT system offers good energy compression, short aid filters, and accurate reconstruction without redundancy. DWT employs an ambiguous noise technique, which gives improved directional discrimination and lower frequency sub-bands. The real picture composition is calculated by magnification and subtraction throughout the multi-resolution process. To keep the information minimal and high frequency, pictures are generally split down into numerous sub-images at numerous resolution levels. The DWT feature allows you to extract texture information from pictures. The internal product f is represented by the squared integral function $f(u)$ and the value (u) is a

function of the real value. The wave function is denoted by eq (18).

$$w[f(s,\tau)] = (f, \psi_{s,t}^k) = \int_{\infty}^{\infty} f(u)\psi_{s,t}^k(u)du$$

(18)

$$Where, \psi_{s,t}^k(u) = \left(\frac{1}{\sqrt{s\psi_{s,t}^k}}/s\right) denotes$$

(19)

Wave family, $s \in z$ is represent as a scale, τ is represent as a translation and $k \in \{h, v, d\}$ is represent as anorientation factors. These have h, v and d represent as a direction correspondingly. The DWT was obtained durings $= 2^j$ and $\tau = 2^j, n, j, n \varepsilon z$. The dyadic wavelet decomposition is a DWT experiment that is scalable; it follows a geometric sequence of ratio 2. The resultant wavelet decomposition makes use of dyadic wavelets applied with impeccable reconstruction filter banks. By the wavelet function $\psi(u)$ and the scaling function $\varphi(u)$ as shown in eq. (8) and (9). Scaling and three mother atoms ψ^h, ψ^v and ψ^d. explain the wavelet atoms. This mother atoms are calculated as the tensor products of 1-dimensional $\psi(u)$ and $\varphi(u)$, as shown in Eq. (20) and (21).

$$\psi_{j,n}^k(u) = \frac{1}{\sqrt{2^j}}\psi^k\left(\frac{u-2^j n}{2^j}\right) \quad (20)$$

$$\varphi_{j,n}^k(u) = \frac{1}{\sqrt{2^j}}\psi^k\left(\frac{u-2^j n}{2^j}\right) \quad (21)$$

$$\varphi(u) = \varphi(u_1)\varphi(u_2), \psi^k(u) \quad (22)$$

$$\psi^v(u) = \varphi(u_1)\psi(u_2), \phi^d(u) \quad (23)$$

A collection of downsamplers and digital filter sets is used to implement the 2-D DWT. A HPF and a HPF are included in the digital filter bank. The original pictures in resolution between the four subband images in vertical, directions are $D_{2^i}^h f, D_{2^i}^h f$ and $D_{2^i}^h f$. The fourth picture is an estimate image, $A_{2^i}f$ discovered at coarse resolution, therefore the complete diseases image A $A_{2^{i+1}}f$ is denoted in the equation (24)

$$A_{2^{i+1}}f = D_{2^i}^h f, +D_{2^i}^v f + D_{2^i}^d f + A_{2^i}f \quad (24)$$

The 2-D orthogonal wavelet is represented by the decomposed sub-images. The wavelet decomposition of a picture yields four orthogonal sub-bands such as Low-Low (LL), Low-High (LH), High-Low (HL) and High-High (HH), which is represented as $D_{2^i}^h f, +D_{2^i}^v f + D_{2^i}^d f$ and $A_{2^i}f$ correspondingly. In this attempt, the essential step of component extraction is LL wavelet highpoints are recovered from each split film employing wavelet clarification, a matrix of contemporaneous gray level events (GLCM) is functional, and the element approximations fade out. Autocorrelation, difference, energy entropy, contrast, uniformity, cluster hue, correlation, uniformity, extreme probability, quantity, variance, normal sum, changes in sum, entropy of sum, fluctuation of difference, entropy conversion are all highlighted registers [31].

3.5. Classification using LSTM and Bi-LSTM

The broken sub-pictures are the 2-D orthogonal wavelet. 4-orthogonal outcomes of the wavelet breaking down of an image RNN has been used with temporal dependence for sequential timeseries [32]. An unfolded RNN can use previous data to process current data. RNN has the challenge in the meantime of training long-term addiction data that is solved in one of the RNN variants. The advance version of the RNN network was employed by LSTM foreseen by Hochreiter & Schmidhuber [33], overcoming the RNN limitations using the hidden layer unit known as memory cells, which store the temporary condition of the network, and which are controlled by three portals: input gate, output gate and forget gate [34]. The work of the input gate and output gate controls the memory cell input and output flow through the remaining network. Moreover, the memory cell was supplied with forgotten gate, which provides high weight output data from the before the next neuron. Memory data relies on the high activation results; the info is stored in the memory cell if the input unit has high activation rates. Furthermore, if the output unit is highly activated, the information is transferred to the following neuron. Otherwise, memory cell input information with high weights.

LSTM network is the calculation map between the input and output sub bands, i.e., $X = (X_1, X_2, \ldots, X_n)$ and $y = (y_1, y_2, \ldots, y_n)$. Calculating by the following equations:

$$f_{orget\,gate} = sigmoid(W_{fg}X_t + W_{hfg}h_{t-1} + h_{fg}) \quad (25)$$

$$i_{nput}g_{ate} = sigmoid(W_{ig}X_t + W_{hig}h_{t-1} + b_{ig})$$
(26)

$$o_{uput}g_{ate} = sigmoid(W_{og}X_t + W_{hog}h_{t\ 1} + b_{og})$$
(27)

$$(\mathcal{C})_t = (\mathcal{C})_{t-1} \otimes (f_{orget}g_{ate})_t +$$
$$(i_{nput}g_{ate})_t \otimes (\tanh(W_i X_t) + W_{hc}h_{t-1} + bc)$$
(28)

$$h_t = o_{uput}g_{ate} \otimes \tanh((\mathcal{C})_{t-1})$$
(29)

In eq. 25, 26, 27, 28 and 29, W_{ig}, W_{og}, W_{hc}, W_{fg} and b_{fg}, b_{ig}, b_{cg}, b_C The three gates and a memory cell represent variables of weights and bias. Here h_{t-1} represents the elemental addition of the previous units of hidden layers with three gates. Upon processing of Eq. 13, the functionality to $(\mathcal{C})_t$ will become the actual cell memory unit. Eq. 29 demonstrates the wise element of the preceding hidden unit output and previous memory unit multiplication. Add the nonlinearity of tanh and sigmoid functions displayed in the eq (25-29) at the top of the three gates. The preceding and current time steps are here $t-1$ and t.

Overcoming the limits of the LSTM cell that can work on past contents but cannot use future contents. Schuster and Paliwal have proposed two different LSTM hidden layers with comparable output in opposed directions to bidirectional recurrent neural networks (BRNN). Earlier and future information is used in the output layer using this design [41]. An input sequence $X = (X_1, X_2, \ldots, X_n)$ in Bi-LSTM is calculated in forward direction as $\vec{h}_t = (\vec{h}_1, \vec{h}_2, \ldots, \vec{h}_n)$ and $\overleftarrow{h}_t = (\overleftarrow{h}_1, \overleftarrow{h}_2, \ldots, \overleftarrow{h}_z$ backward directions as. This cell yt is formed by both $\overleftarrow{h}_t$ and $\vec{h}_t$, the final order of out looks like $y = (y_1, y_2, \ldots, y_n)$ .Fig. 4shows the single cell of Bi-LSTM.
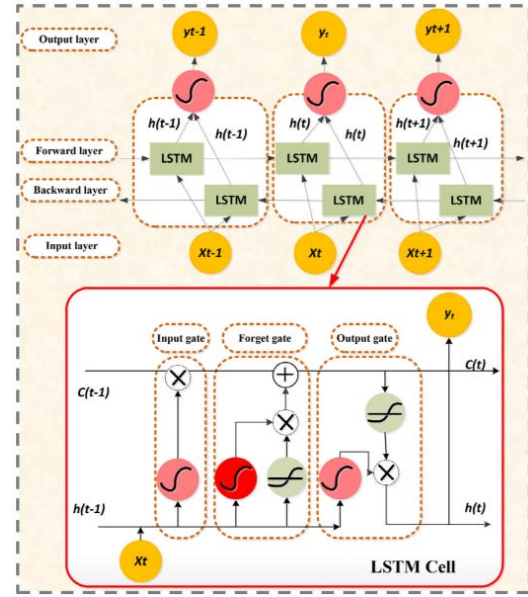

Figure 4: single LSTM cell and Bi-LSTMArchitecture

4. Results and discussion

MATLAB (version 2018a) with Intel i3 3.0 GHz processor, and 8 GB RAM are experimenting with the proposed system. In comparison with existing methods on reputable data sets like PLOC and Kaggle, the efficiency is measured using the suggested system. In the PLOC dataset 150 images are trained and 50 images are tested for each class. In the Kaggle dataset 200 images are trained and 75 images are tested for each class.

4.1. Segmentation Evaluation

The challenge assessment metrics are used to assess our method's performance in segmentation and classification. Sensitivity (SE), accuracy (AC), Jaccard index (JSI)specificity (SP) and Dice coefficient (DSC) are the evaluation factors for segmentation).The performance standards are distinct is as:

$$SE = \frac{tp}{tp+fn}$$
(30)

$$SP = \frac{tn}{tn+fp}$$
(31)

$$AC = \frac{tp-tn}{tp+fp+tn+fn}$$
(32)

$$DSC = \frac{2TP}{(2TP+FP+FN)}$$
(33)

$$JSI = \frac{TP}{FP+FN+TP}$$
(34)

The number of true positives, false positives, true negatives and false negatives is denoted by tp, tn, fp and fn. The definitions of SE, SP, and AC are the same as for segmentation metrics, but they are measured at the picture level rather than the pixel level. The number of endometrial carcinoma and non-endometrial carcinoma lesions in the testing dataset is significantly unbalanced in the classification job. In this situation, the FPR should be low while the actual negative rate should be high. The picture 5 depicts some of the sample segmented photos from the PLOC dataset.
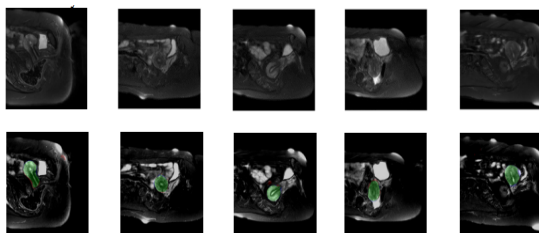

Figure 5: Sample proposed segmentation applied Images.

Table 2 displays the comparative analysis of proposed segmentation method for both datasets. Figure 6 and 7 shows the graphical representation of proposed TGVFCMS for both datasets.

Reference	Average of evaluation metrics				
	DSC	JSI	Acc	Sens	Spec
Silveira.et al.[36]	0.920	--	--	0.930	0.950
N. Z. Tajeddin, and B. M. Asl, [37]	0.910	0.878	0.955	0.941	0.971
FCM segmentation (PLOC dataset)	0.910	0.847	0.918	0.914	0.960
FCM segmentation (Kaggle dataset)	0.831	0.676	0.858	0.872	0.907
Proposed System (PLOC dataset)	**0.945**	**0.89**	**0.961**	**0.971**	**0.983**
Proposed System (Kaggle dataset)	**0.931**	**0.90**	**0.936**	**0.961**	**0.975**

Table.2. Evaluation and comparison of the proposed segmentation.

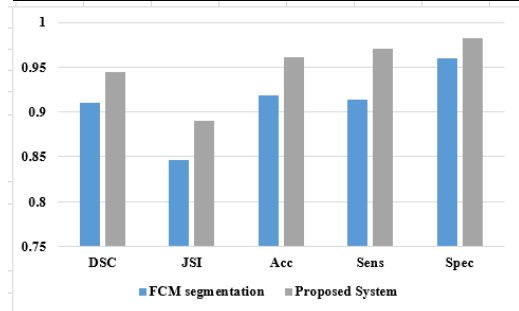| S. no	Ref	Sensitivity (%)	Specificity (%)	Accuracy (%)
1	Pennisi et al. [38] (2016)	93.15	88.41	--
2	Barata et al. [39] (2015)	91.52	77.30	85.3
3	Sateesha et al. [40] (2017)	93.48	96.12	--
4	S. Pathan, *et al.,* [41] (2019)	94.67	84.57	89.10
5	. Z. Tajeddin, and B. M. sl, [37] (2018)	95.67	96.64	95.70
6.	S. Pathan, *et al,* [42] (2018)	84.60	89.7	88.17
7.	S. Pathan, *et al.,* [43] (2017)	85.71	83.25	84.16
8	Proposed LSTM and Bi-LSTM	**97.00**	**98.50**	**97.10**

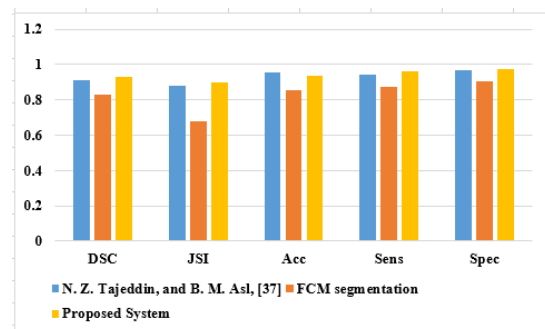**Figure 6:** Graphical Representation of Proposed Segmentation Technique for PLOC dataset

Figure 7: Graphical Representation of Proposed Segmentation Technique for Kaggle dataset

The provided values are the mean of 200 segmentation assessment indicators. Silveira et al. [36] offered many approaches for endometrium lesion segmentation; we present their best-performing technique. N. Z. Tajeddin and B. M. Asl developed a segmentation method with an average accuracy of 95.5 percent [37]. In addition, high values of likeness coefficients for segmentation outputs have been recorded, such as DSC of 91 percent and JSI of 87.8 percent, respectively. The existing FCM technique achieved better performance in terms of all parameters for PLOC datasets than Kaggle datasets. The proposed segmentation technique (TGVFCMS-MWOA) achieved 94.5% of DSC, 89% of JSI, 96.1% of accuracy, 97% of Sens and 98.3% of Spec for PLOC dataset. The same proposed method achieved 93.1% of DSC, 90% of JSI, 93.6% of accuracy, 96.1% of Sens and 97.5% of Spec for Kaggle dataset. This proves that the proposed scheme has improved performance in PLOC dataset. The next section shows the presentation of proposed classifiers with existing techniques on two datasets.

4.2. Classification Performances

The proposed LSTM and Bi-LSTM are verified against extant methods using many factors, which are described in this section. The assessment metrics are there to evaluate the property of the LSTM and Bi-LSTM system to hands-on advancement methods. It is the set of measurements that survey a shared original attitude of evaluation. Sensitivity, specificity, and accuracy were chosen as assessment measures. Table 2 compares potential classifiers for endometrium lesion categorization and graphical representations are presented in Figure 7 and 8.
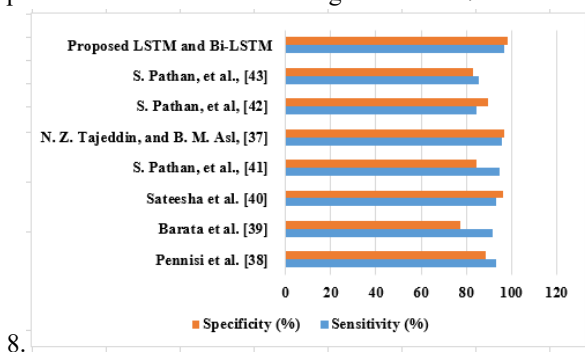

Figure 8: Graphical Representation of Proposed Classifiers in terms of Specificity and Sensitivity
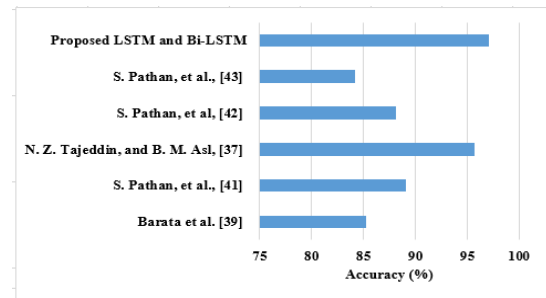

Figure 9: Graphical Representation of Proposed Classifiers in terms of Accuracy

Pennisi et al. classified benign and malignant tumors using a mix of geometric and color characteristics [38]. The technique, however, is sensitive to pictures with uneven borders, especially tumors with unusual network and reticular patterns. Furthermore, the technique is unsuitable for diagnostic applications and needs additional improvement before being used in a CAD system. Barata et al. suggested a bag of characteristics method in combination with color constancy models for identifying benign and malignant lesions, obtaining an accuracy of 83.4 percent [39]. Color constancy procedures are susceptible to capturing device changes. Sateesha et al. has presented a 3D lesion reconstruction approach for melanocytic lesion categorization [40]. The technique makes use of a collection of color texture and form characteristics, as well as rough estimations of lesion depths. However, the design's primary challenges include computational complexity and refinement in the depth estimation approach. These existing techniques achieved 85% to 96% of accuracy, sensitivity, and specificity. But the proposed LSTM and Bi-LSTM achieved 97% of sensitivity, 98.50% of specificity and 97.10% of accuracy. This shows that the proposed technique achieved better presentation than existing techniques. This experimental analysis proved that the proposed technique effectively classifies the endometrium lesions from both datasets.

5. Conclusion

Endometrial carcinoma is the fastest-growing types of endometrium cancer, therefore early identification is critical. Early detection is beneficial and can offer strong recommendations for specific and appropriate treatment regimens. In this paper, we presented a technique for detecting endometrial carcinoma endometrium cancer. The suggested approach consists of four stages: tumor detection and segmentation using pre-processing techniques, endometrium lesions segmentation using

TGVFCMS-MWOA, and endometrial carcinoma diagnosis using deep learning techniques to extract features from endometrium lesions. The HLOG filter is quite effective for detecting tumors. The TGVFCMS-MWOA is highly effective in detecting endometrium lesions with low intensity, and it also removes shadow and shading effects. The studies are conducted on two datasets, PLOC and Kaggle, although Kaggle pictures exhibit lower accuracy and DSI when compared to PLOC datasets. In the future, we want to study and fuse feature selection models with the specific characteristics used here for endometrial carcinoma endometrium cancer diagnosis to enhance the accuracy of each job, and we intend to execute the training process on a wider collection of pictures acquired from various places.

Reference

[1]. American Cancer Society. Global Cancer Facts & Figures, 4th ed.; American Cancer Society: Atlanta, GA, USA, 2018.

[2]. Lortet-Tieulent, J.; Ferlay, J.; Bray, F.; Jemal, A. International patterns and trends in endometrial cancer incidence, 1978–2013. J. Natl. Cancer Inst. 2018, 110, 354–361. [CrossRef] SGO Clinical Practice Endometrial Cancer Working Group; Burke, W.M.; Orr, J.; Leitao, M.; Salom, E.;

[3]. Gehrig, P.; Olawaiye, A.B.; Brewer, M.; Boruta, D.; Herzog, T.J.; et al. Endometrial cancer: A review an current management strategies: Part I. Gynecol. Oncol. 2014, 134, 385–392. [CrossRef]

[4]. 4. SGO Clinical Practice Endometrial Cancer Working Group; Burke, W.M.; Orr, J.; Leitao, M.; Salom, E.; Gehrig, P.; Olawaiye, A.B.; Brewer, M.; Boruta, D.; Herzog, T.J.; et al. Endometrial cancer: A review and current management strategies: Part II. Gynecol. Oncol. 2014, 134, 393–402. [CrossRef]

[5]. Colombo, N.; Creutzberg, C.L.; Amant, F.; Bosse, T.; González-Martín, A.; Ledermann, J.; Marth, C.; Nout, R.; Querleu, D.; Mirza, M.; et al. ESMO-ESGO-ESTRO consensus conference on endometrial cancer: Diagnosis, treatment and follow-up. Int. J. Gynecol. Cancer 2016, 26, 2–30. [CrossRef]

[6]. Meissnitzer, M.; Forstner, R. MRI of endometrium cancer—How we do it. Meissnitzer Forstner Cancer Imaging 2016, 16, 11. [CrossRef]

[7]. Larson, D.M.; Connor, G.P.; Broste, S.K.; Krawisz, B.R.; Johnson, K.K. Prognostic significance of gross myometrial invasion with endometrial cancer. Obstet. Gynecol. 1996, 88, 394–398. [CrossRef]

[8]. Mitamura, T.; Watari, H.; Todo, Y.; Kato, T.; Konno, Y.; Hosaka, M.; Sakuragi, N. Lymphadenectomy can be omitted for low-risk endometrial cancer based on preoperative assessments. J. Gynecol. Oncol. 2014, 25, 301–305. [CrossRef] [PubMed]

[9]. Alcázar, J.L.; Gastón, B.; Navarro, B.; Salas, R.; Aranda, J.; Guerriero, S. Transvaginal ultrasound versus magnetic resonance imaging for preoperative assessment of myometrial infiltration in patients with endometrial cancer: A systematic review and meta-analysis. J. Gynecol. Oncol. 2017, 28, e86. [CrossRef] [PubMed]

[10]. Hricak, H.; Rubinstein, L.V.; Gherman, G.M.; Karstaedt, N. MR imaging evaluation of endometrial carcinoma: Results of an NCI cooperative study. Radiology 1991, 179, 829–832. [CrossRef] [PubMed]

[11]. Choi, H.-J.; Lee, S.; Park, B.K.; Kim, T.-J.; Kim, C.K.; Park, J.J.; Choi, C.H.; Lee, Y.-Y.; Lee, J.-W.; Bae, D.-S.; et al Long-term outcomes of magnetic resonance imaging-invisible endometrial cancer. J. Gynecol. Oncol. 2016, 27, e38. [CrossRef]

[12]. Bi, W.L.; Hosny, A.; Schabath, M.B.; Giger, M.L.; Birkbak, N.J.; Mehrtash, A.; Allison, T.; Arnaout, O.; Abbosh, C.; Dunn, I.F.; et al. Artificial intelligence in cancer imaging: Clinical challenges and applications. CA Cancer J. Clin. 2019, 69, 127–157. [CrossRef] [PubMed]

[13]. Weidlich, V.; Weidlich, G.A. Artificial intelligence in medicine and radiation oncology. Cureus 2018, 10, e2475. [CrossRef] [PubMed]

[14]. Mendelson, E.B. Artificial intelligence in breast imaging—Potentials and limitations. AJR Am. J. Roentgenol. 2019, 212, 293–299. [CrossRef] [PubMed]

[15]. Hwang, D.-K.; Hsu, C.-C.; Chang, K.-J.; Chao, D.; Sun, C.-H.; Jheng, Y.-C.; Yarmishyn, A.A.; Wu, J.-C. Tsai, C.-Y.; Wang, M.-L.; et al. Artificial intelligence-based decision-making for age-related macular degeneration. Theranostics 2019, 9, 232–245. [CrossRef]

[16]. Esteva, A.; Kuprel, B.; Novoa, R.A.; Ko, J.; Swetter, S.M.; Blau, H.M.; Thrun, S. Dermatologist-level classification of skin cancer with deep neural networks. Nature 2017, 542, 115–118. [CrossRef]

[17]. Litjens, G.; Kooi, T.; Bejnordi, B.E.; Setio, A.A.A.; Ciompi, F.; Ghafoorian, M.; Van Der Laak, J.A.; Van Ginneken, B.; Sánchez, C.I. A survey on deep learning in medical image analysis. Med. Image Anal. 2017, 42, 60–88. [CrossRef]

[18]. Doupe P, Faghmous J, Basu S. Machine learning for health services researchers. Value Health. 2019;22(7):808-815. Available from: https://pubmed.ncbi.nlm.nih.gov/31277828/ [Accessed: October 1, 2020]

[19]. Crown WH. Potential application of machine learning in health outcomes research and some statistical cautions. International Society for Pharmacoeconomics and Outcomes Research (ISPOR). 2015. DOI: 10.1016/j.jval.2014.12.005 [Accessed: October 1, 2020]

[20]. Ghassemi M, Naumann T, Schulam P, Beam AL, Chen IY, Ranganath R. A review of challenges and opportunities in machine learning for health. arXivLabs. 2019. Available from: https://arxiv.org/abs/1806.00388 [Accessed: October 1, 2020]

[21]. Buch VH, Ahmed I, Maruthappu M. Artificial intelligence in medicine: Current trends and future possibilities. British Journal of General Practice. 2018;68(668):143-144. DOI: 10.3399/bjgp18X695213 [Accessed: October 1, 2020]

[22]. Rajkomar A, Lingam S, Taylor AG, Blum M, Mongan J. High-throughput classification of radiographs using deep convolutional neural networks. Journal of Digital Imaging. 2016;30:95-101. DOI: 10.1007/s10278-016-9914-9

[23]. Chen M, Hao Y, Hwang K, Wang L, Wang L. Disease prediction by machine learning over big data from healthcare communities. IEEE. 2017;5:8869-8879. DOI: 10.1109/ACCESS.2017.2694446 [Accessed: October 1, 2020]

[24]. Alexandru AG, Radu IM, Bizon ML. Big data in healthcare—Opportunities and challenges. Informatica Economică. 2018;22(2):43-54. DOI: 10.12948/issn14531305/22.2.2018.05

[25]. E. Endometriosis: Advances and controversies in classification, pathogenesis, diagnosis, and treatment. Version 1. F1000Research. 2019;8:F1000. DOI: 10.12688/f1000research.14817.1. Available from: https://www.ncbi.nlm.nih.gov/pmc/articles/PMC6480968/ [Accessed: March 30, 2021]

[26]. Chapron C, Fauconnier A, Goffinet F, Breart G, Dubuisson JB. Laparoscopic surgery is not inherently dangerous for patients presenting with benign gynaecologic pathology. Results of a meta-analysis. Human Reproduction. 2002;17:1334-1342

[27]. Parasar P, Ozcan P, Terry KL. Endometriosis: Epidemiology, diagnosis and clinical management. Current Obstetrics and Gynecology Reports. 2017;6(1):34-41. DOI: 10.1007/s13669-017-0187-1

[28]. Hoogeveen M, Dorr PJ, Puylaert JBCM. Endometriosis of the rectovaginal septum: Endovaginal US and MRI findings in two cases. Abdominal Imaging. 2020;28:897-901

[29]. Akter S, Xu D, Nagel SC, Bromfield JJ, Pelch KE, Wilshire GB, et al. GenomeForest: An ensemble machine learning classifier for endometriosis. AMIA Joint Summits on Translational Science proceedings. 2020;2020:33-42

[30]. Sadia A, Dong X, Nagel Susan C, Bromfield John J, Katherine P, Wilshire Gilbert B, et al. Machine learning classifiers for

endometriosis using transcriptomics and methylomics data. Frontiers in Genetics. 2019;10:766. DOI: 10.3389/fgene.2019.00766

[31]. Nnoaham KE, Hummelshoj L, Kennedy SH, Jenkinson C, Zondervan KT, World Endometriosis Research Foundation Women's Health Symptom Survey Consortium. Developing symptom-based predictive models of endometriosis as a clinical screening tool: Results from a multicenter study. Fertility and Sterility. 2012;98(3):692-701.e5. DOI: 10.1016/j.fertnstert.2012.04.022. Epub 2012 May 30

[32]. Noventa M, Saccardi C, Litta P, Vitagliano A, D'Antona D, Abdulrahim B, et al. Ultrasound techniques in the diagnosis of deep pelvic endometriosis: Algorithm based on a systematic review and meta-analysis. Fertility and Sterility. 2015;104(2):366-383.e2. DOI: 10.1016/j.fertnstert.2015.05.002

[33]. Zhang Y, Wang Z, Zhang J, et al. Deep learning model for classifying endometrial lesions. Journal of Translational Medicine. 2021;19:10. DOI: 10.1186/s12967-020-02660-x

[34]. Endometriosis signs and symptoms. Available from: https://www.hopkinsmedicine.org/health/conditions-and-diseases/endometriosis [Accessed: October 1, 2020]

[35]. PRA Health Sciences. Data Insights. Available from: https://prahs.com/healthcare-intelligence/data-insights

[36]. Symphony Health Solutions. Available from: https://symphonyhealth.prahs.com/

[37]. N. Z. Tajeddin, and B. M. Asl. "Endometrial carcinoma recognition in dermoscopy images using lesion's peripheral region information." Computer methods and programs in biomedicine 163 (2018): 143-153.

[38]. A. Pennisi, D.D. Bloisi, D. Nardi, A.R. Giampetruzzi, C. Mondino, A. Facchiano, Endometrium lesion image segmentation using Delaunay Triangulation for endometrial carcinoma detection, Comput. Med. Imaging Graphics 52 (2016) 89–103.

[39]. C. Barata, M.E. Celebi, J.S. Marques, Improving dermoscopy image classification using color constancy, IEEE J. Biomed. Health Inf. 19 (3) (2015) 1146–1152.

[40]. T. Y. Satheesha, Satyanarayana, D., Prasad, M. G., &Dhruve, K. D. (2017). Endometrial carcinoma is endometrium deep: a 3D reconstruction technique for computerized Magnetic Resonance endometrium lesion classification. IEEE journal of translational engineering in health and medicine, 5, 1-17.

[41]. S. Pathan, K. Gopalakrishna Prabhu, and P. C. Siddalingaswamy. "Automated detection of melanocytes related pigmented endometrium lesions: A clinical framework." Biomedical Signal Processing and Control 51 (2019): 59-72.

[42]. S. Pathan, K. Gopalakrishna Prabhu, and P. C. Siddalingaswamy. "A methodological approach to classify typical and atypical pigment network patterns for endometrial carcinoma diagnosis." Biomedical Signal Processing and Control 44 (2018): 25-37.

[43]. S. Pathan, Siddalingaswamy, P. C., Lakshmi, L., & Prabhu, K. G. (2017, September). Classification of benign and malignant melanocytic lesions: A CAD tool. In 2017 International Conference on Advances in Computing, Communications and Informatics (ICACCI) (pp. 1308-1312). IEEE.

[44]. Gohagan, J.K., Prorok, P.C., Hayes, R.B., Kramer, B.S.: The prostate, lung, colorectal and ovarian (plco) cancer screening trial of the national cancer institute: history, organization, and status. Controlled clinical trials 21(6) (2000) 251S–272S

Satya Kiranmai Tadepalli is currently working as an Assistant professor in Chaitanya Bharathi Institute of Technology(A), Hyderabad, Telangana, India. Her research interest includes Machine Learning, Artificial Intelligence.

Prof. P.V.Lakshmi is with the Department of Computer Science & Engineering, GITAM (Deemed to be University), A.P, India. She is former HOD and member of Academic council .
Her research interests includes Discrete Mathematics, Cryptography, Network security, Algorithm in Bioinformatics. She has more than 21+ years of teaching experience. She has authored several technical papers, conducted workshops, conferences and seminars, and published two books and is editor for springer brief titled "Computational Intelligence Techniques in Health Care".She has completed one project funded by UGC as Principle Investigator. She has reviewed technical papers and was Technical Program Committee Co-Chair of international conferences. She is Life member of Cryptology Society of India, Member of Bioinformatics.Org, Member of IEEE, Life Member of Computer Society of India and Member of IETE.